Comparison between a Two-Wavelength Absolute Distance Meter and a GNSS-Based Distance Meter at CERN Geodetic Network

Joffray Guillory, Ph.D.[1]; Sergio Baselga, Ph.D., M.ASCE[2]; Jean-Pierre Wallerand, Ph.D.[3]; Daniel Truong[4]; Luis García-Asenjo, Ph.D.[5]; Raquel Luján[6]; Damien Pesce[7]; Benjamin Weyer[8]; Jean-Frederic Fuchs[9]; and Dominique Missiaen[10]

Abstract: Absolute distance determination, which is the determination of distances consistent with the International System of Units (SI) definition of meter, is a current challenge for distances of several kilometers in the open air and with submillimetric accuracies, which is being increasingly demanded for scientific and technological applications. We present the first comparison of two techniques recently developed for this purpose: the Arpent Absolute Distance Meter and the improved Global Navigation Satellite System (GNSS)-based distance meter. Both techniques have been tested and compared on the European Organization for Nuclear Research (CERN) geodetic network during a 2-week observation campaign. The results obtained include the rigorous determination of the uncertainties for both methodologies. In the end, four baselines of 2.2, 4.8, 6.0, and 6.5 km were measured, and for three of them, the differences between the two systems were less than 0.7 mm. The baseline of 4.8 km showed a difference of 2.7 mm, i.e., about 0.6 parts per million (ppm): in the case of conventional optical telemetry, such an agreement would require refractivity correction with knowledge of the air temperature and pressure at better than 0.6 K and 0.15 hPa, respectively. **DOI: 10.1061/JSUED2.SUENG-1523.**

Author keywords: Length metrology; Optical distance meters; Global Navigation Satellite System (GNSS); Refractive index compensation.

Introduction

In fields such as geodesy, civil engineering, or deformation monitoring, where a well-controlled scale is crucial, there is a growing demand for distance measurements over several kilometers with submillimetric accuracy (Pollinger et al. 2023). This includes the survey of the European Organization for Nuclear Research (CERN) geodetic network, which will be extended for the eventual construction of the Future Circular Collider (FCC), the monitoring of calibration baselines, and the determination of local ties. To this end, novel instruments have been developed and improved in recent years, such as the two-wavelength absolute distance meter (ADM) from the Conservatoire national des arts et métiers (Cnam), called Arpent (Guillory et al. 2024), and the improved Global Navigation Satellite System (GNSS)-based distance meter (GBDM+) from Universitat Politècnica de València (UPV) (Baselga et al. 2022). The two systems follow completely different approaches, one being optical and the other being GNSS-based. However, both aim to

[1]Research Engineer, Conservatoire National des Arts et Métiers (Cnam), Laboratoire commun de métrologie LNE-Cnam, 1 Rue Gaston Boissier, Paris 75015, France (corresponding author). ORCID: https://orcid.org/0000-0002-0325-1695. Email: joffray.guillory@cnam.fr

[2]Professor, Departamento de Ingeniería Cartográfica, Geodesia y Fotogrametría, Universitat Politècnica de València, Camino de Vera s/n, Valencia 46022, Spain. ORCID: https://orcid.org/0000-0002-0492-4003. Email: serbamo@cgf.upv.es

[3]Research Engineer, Conservatoire National des Arts et Métiers (Cnam), Laboratoire commun de métrologie LNE-Cnam, 1 Rue Gaston Boissier, Paris 75015, France. Email: jean-pierre.wallerand@cnam.fr

[4]Technical Engineer–Two-Year University Degree, Conservatoire National des Arts et Métiers (Cnam), Laboratoire commun de métrologie LNE-Cnam, 1 Rue Gaston Boissier, Paris 75015, France. Email: daniel.truong@cnam.fr

Note. This manuscript was submitted on March 7, 2024; approved on July 1, 2024; published online on October 9, 2024. Discussion period open until March 9, 2025; separate discussions must be submitted for individual papers. This paper is part of the *Journal of Surveying Engineering*, © ASCE, ISSN 0733-9453.

[5]Associate Professor, Departamento de Ingeniería Cartográfica, Geodesia y Fotogrametría, Universitat Politècnica de València, Camino de Vera s/n, Valencia 46022, Spain. ORCID: https://orcid.org/0000-0001-6535-2216. Email: lugarcia@cgf.upv.es

[6]Ph.D. Student, Departamento de Ingeniería Cartográfica, Geodesia y Fotogrametría, Universitat Politècnica de València, Camino de Vera s/n, Valencia 46022, Spain. ORCID: https://orcid.org/0000-0002-6300-0409. Email: ralugar@cgf.upv.es

[7]Surveying Technician–Two-Year University Degree, Institut national de l'information géographique et forestière (IGN), Service de géodésie et de métrologie, 73 Ave. De Paris 94165 Saint-Mandé CEDEX, France. Email: damien.pesce@ign.fr

[8]Surveying Engineer, Acquisition Processing and Data Control Software Section, Beam Dept. —Geodetic Metrology Group, European Organization for Nuclear Research (CERN), Geneva CH-1211, Switzerland. Email: benjamin.weyer@cern.ch

[9]Surveying Engineer, Accelerator Survey and Geodesy Section, Beam Dept. —Geodetic Metrology Group, European Organization for Nuclear Research (CERN), Geneva CH-1211, Switzerland. Email: jean-frederic.fuchs@cern.ch

[10]Surveying Engineer, Site and Civil Engineering Dept. —Topography and Geomatics, European Organization for Nuclear Research (CERN), Geneva CH-1211, Switzerland. Email: dominique.missiaen@cern.ch

determine lengths traceable to the International System of Units (SI) definition of the meter, with uncertainties of 1 mm or less for a coverage factor k of 2 and distances of at least 5 km. To achieve the desired accuracy, the ADM must reduce the effect of the air refractive index. For this purpose, it measures distances using laser beams at two different wavelengths. For the GBDM+, the essential element was the development of an improved GNSS-based methodology that includes the characterization of all the sources of error, with correction and estimation of uncertainty at the zero-difference level and the propagation of all the estimated uncertainties to the final distance.

The two methods are very different in nature. The ADM requires direct intervisibility between the endpoints, as for a conventional electro-optic distance meters (EDMs), whereas the GBDM+ requires a clear horizon in the surroundings of the station to avoid signal obstruction and multipath. The maximum range of the ADM is limited by the powers emitted by the lasers, whereas the GBDM+ is limited by the possible inaccuracies of the observation model, which increase with distance. In addition, the difficulty in obtaining the total uncertainty in GNSS as a result of the individual uncertainties of all the contributing sources is usually considered to be a major limitation of this technique. Finally, the ADM measurement can be carried out in a few minutes, whereas GBDM+ requires a significant integration time of a few days, mainly to characterize the multipath effect.

The main objective of this article is to present the first comparison of these two techniques and to quantify the compatibility of their results. To this end, the geodetic network of CERN was used to compare these novel instruments. This network consists of about 40 geodetic pillars spread across the CERN site (Jones and Missiaen 2018). Most of the pillars used for our comparison were created for the construction of the Large Electron-Positron Collider (LEP), a large particle accelerator of 27-km circumference located on the French–Swiss border, near Geneva, Switzerland. Such a large-scale scientific instrument required the use of high-precision distance meters for its installation, alignment, and monitoring. Indeed, the CERN geodetic network has been regularly measured from the 1980s to the present days using various techniques such as GNSS or EDM.

In 1983, the Terrameter LDM-2, an ADM able to compensate for the air refractive index (Gervaise 1983; Huggett 1981) was also used to survey the CERN geodetic network. Distances ranging from 3.5 to 13.6 km were measured with an uncertainty of 1 mm over 10 km. However, no commercial version of such ADMs exists. Thus, developments are underway (Minoshima et al. 2011; Röse et al. 2022; Ray et al. 2023) to propose successors based on modern optics and electronics that are robust, transportable, and traceable to the SI. The ADM developed by Cnam is one of these new instruments: it has demonstrated through a rigorous uncertainty budget that it can measure distances with a submillimetric uncertainty. The purpose of this paper is to confirm the performance of this ADM by comparing it with GBDM+, a system that is totally different in nature.

The paper is structured as follows. First, the methodology for the comparison carried out on the CERN geodetic network is presented. The next section presents the two-wavelength ADM and the measurements carried out with this instrument. An uncertainty budget is also reported. The following sections are the equivalent to the previous section for the GBDM+ system and the single-wavelength EDM. The results of the different techniques are then compared and analyzed in the subsequent section.

Methodology

The comparison between the Cnam ADM and the UPV GBDM+ took place over 2 weeks. As shown in Fig. 1, four baselines with lengths between 2.2 and 6.5 km have been measured using a subset of five pillars of the CERN geodetic network. These measurements were carried out in different steps, with the help of Institut national de l'information géographique et forestière (IGN) and the support of CERN:

- Two-wavelength ADM measurements between July 4 and 8, 2022 (first week).
- GBDM+ measurements between July 11 and 14, 2022 (second week).
- In addition, on July 14, 2022, further measurements were made with a single-wavelength EDM [Kern Mekometer ME5000 (Kern & Co. AG, Aarau, Switzerland)] to demonstrate the advantage of our new instruments.

To ensure accurate distance comparison, it is crucial to compare the same measurands. In the present case, these are geometric distances between two geodetic marks. As the pillars of the CERN geodetic network are equipped with CERN sockets (Appendix II), the reference marks used were centered on the top edge of the socket bores. The ADM, its retroreflector, but also the GNSS antennas, were all equipped with a Leica (Leica Geosystems, Heerbrugg, Switzerland) carrier or equivalent. Leica Tribrachs mounted on forced-centering mounts were therefore used as adapters. These adapters were installed on the different pillars for the entire 2-week measurement campaign, ensuring that all instruments used the same setup for a given pillar. In all the cases, the leveling of the instruments was realized adjusting the thumbscrews of the Tribrachs.

Two-Wavelength ADM: Arpent

Principle

The main challenge for optical distance meters is the determination of the air refractive index n. Usually it is calculated using a semiempirical equation, such as those of Edlén (1966), or Ciddor and Hill (1999) recommended by the International Association of Geodesy (IAG 1999). These equations depend on the vacuum optical wavelength λ, but also on the air temperature T, the pressure p, the partial pressure of water p_ω, and the CO_2 content x_{CO2}. These atmospheric parameters must therefore be measured carefully in order to estimate their value as accurately as possible along the line of sight, preferably at the same time as the distance measurement, especially the temperature and the pressure because they contribute greatly to the light velocity. For example, at the operating wavelength of the Mekometer ME5000, i.e., 632.8 nm, and under a standard air with $T = 20°C$, $p = 1{,}013.25$ hPa, relative humidity (RH) $= 50\%$, and $x_{CO2} = 420$ parts per million (ppm), an error of 1 K in the temperature value or 3.7 hPa in the pressure value will cause an error in the measured distance of 1 ppm.

To avoid temperature and pressure measurements, a solution consists in simultaneously measuring a distance with two different wavelengths, λ_1 and λ_2. The dispersion between these wavelengths results in two distinct measurements of optical path lengths, D_1 and D_2, and ultimately enables the calculation of an air-index compensated distance L

$$L = D_1 - A(\lambda_1, \lambda_2) \times (D_2 - D_1) \tag{1}$$

where $L = D_1/n(\lambda_1, T, p, x, p_\omega) = D_2/n(\lambda_2, T, p, x, p_\omega)$; and A = factor that is considerably less sensitive to the environmental parameters, and even constant in dry air

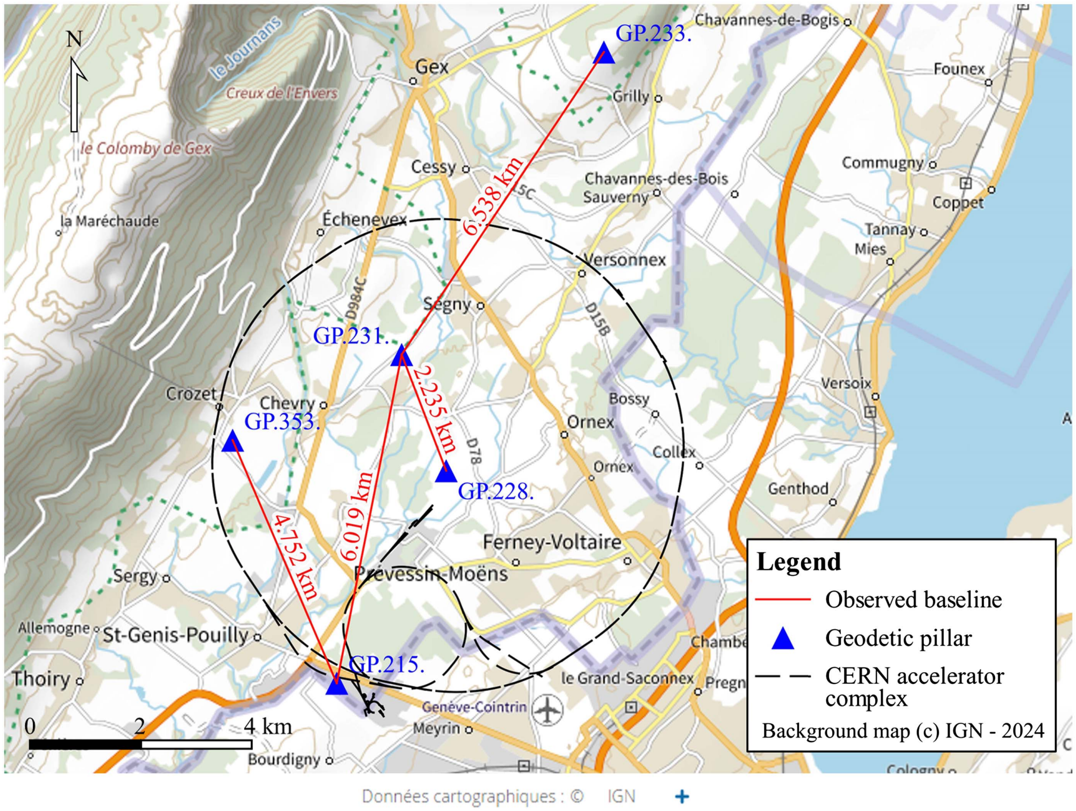

Fig. 1. Map of the CERN accelerator complex. The five pillars used, which form part of the geodetic network, are labeled with their respective identifier. The four baselines are also indicated, along with their lengths (km). (Map Source: © IGN.)

$$A(\lambda_1, \lambda_2) = \frac{n(\lambda_1, T, p, x, p_\omega) - 1}{n(\lambda_2, \ldots) - n(\lambda_1, \ldots)} \underset{\text{dry air}}{=} \frac{K(\lambda_1)}{K(\lambda_2) - K(\lambda_1)} \quad (2)$$

Meiners-Hagen and Abou-Zeid (2008) showed, using the equation of Bönsch and Potulski (1998), an updated version of the Edlén's equation, that the dependence of the air-index compensated distance on air temperature and atmospheric pressure is still removed for moist air, only the dependence on the partial pressure of water vapor remains

$$L = \frac{K(\lambda_1)D_2 - K(\lambda_2)D_1}{K(\lambda_1) - K(\lambda_2) + p_\omega \times (g(\lambda_1) \cdot K(\lambda_2) - g(\lambda_2) \cdot K(\lambda_1))} \quad (3)$$

where $K(\lambda)$ and $g(\lambda)$ = dispersion and humidity terms (see Edlén's equation). Eq. (3) shows that air humidity must always be measured and corrected. In practice, partial pressure of water vapor is determined by measuring relative humidity and temperature. As will be explained subsequently, local measurements of these parameters are sufficient to obtain, over 6.5 km, an uncertainty contribution from humidity of less than 0.2 mm over the air-index compensated distance (assuming that the terrain is uniform between the two baseline endpoints).

Cnam has developed its own version of a two-wavelength ADM (Guillory et al. 2024). It operates at 780 and 1,560 nm with a factor A of about 48. For each wavelength λ_i, an optical beam is continuously propagated in the air from the ADM to an optical retroreflector, then returned to the instrument. The intensity of each of these beams is modulated by a sinusoidal wave using a radio frequency (RF) synthesizer at f_{RF} equal to 5 GHz. Thus, the phase difference $\Delta\phi_{RF}(\lambda_i)$ between the transmitted and received amplitude-modulated continuous wave (AM-CW) is proportional to the optical path length D_i

$$D_i = \frac{1}{2} \times \left(\frac{\Delta\phi_{RF}(\lambda_i)}{2\pi} + k_i \right) \times \frac{c}{f_{RF}} \quad (4)$$

where c = speed of light in vacuum. The measured RF phase difference is wrapped into the interval $[-\pi, +\pi]$. The number of times that this phase has rotated by 2π during its propagation corresponds to the integer k_i. It is determined in practice by measuring the optical path length for different frequencies.

The instrument developed by Guillory et al. (2024) is shown in Fig. 2. The two optical beams are generated inside the ADM, then transmitted by optical fibers to an optical head where they are combined and collimated for propagation over long distances. This head is a gimbal mechanism designed so that the optical beams pass through its invariant point of rotation. Similarly, the distant target is a gimbal mechanism with a hollow corner cube whose center is located at its invariant point of rotation. Finally, after a round trip in the air of several kilometers, the two signals return to the ADM to be detected by high-speed photodiodes, then processed by a phasemeter. A computer finally calculates the optical path lengths.

Measurement of the Baseline Lengths

During the measurement campaign, the two optical beams of the ADM were not perfectly aligned, and it was difficult to obtain a signal for both wavelengths simultaneously, especially for long-distance measurements. This resulted in a low number of points recorded. For example, for the distance of 6.5 km, only 1 in 10,000 measurements had a level of RF signals higher than −15 dB m for both wavelengths simultaneously. This problem was resolved after

J. Surv. Eng., 2025, 151(1): 04024014

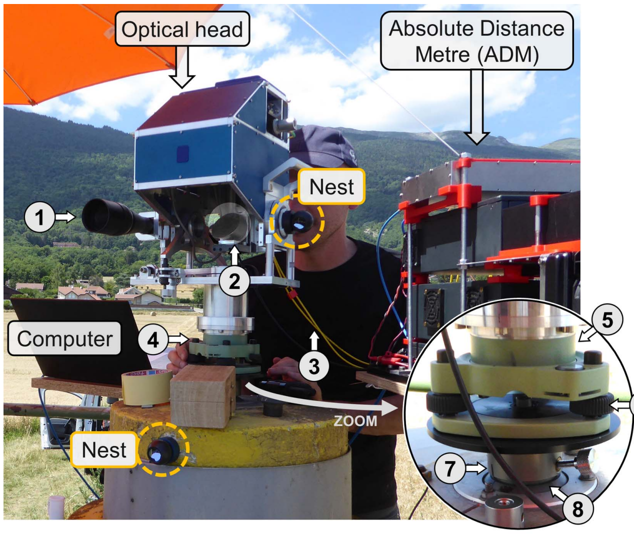

Fig. 2. Instrument installed on Pillar 351, along with the computer used for distance measurement and 38.1 mm (1.5-in.) nests equipped with spherically mounted retroreflectors (SMR) and used for instrument height determination. 1 = scope used for aiming the distant target, 2 = main parabolic mirror used for beam collimation, 3 = two optical fibers, one per wavelength, between the two-wavelength ADM and the optical head, 4 = mounting of the head on the pillar, which benefits from a zoom, 5 = Leica carrier, 6 = Tribrach and its thumbscrews for leveling, 7 = forced-centering mount, and 8 = CERN socket.

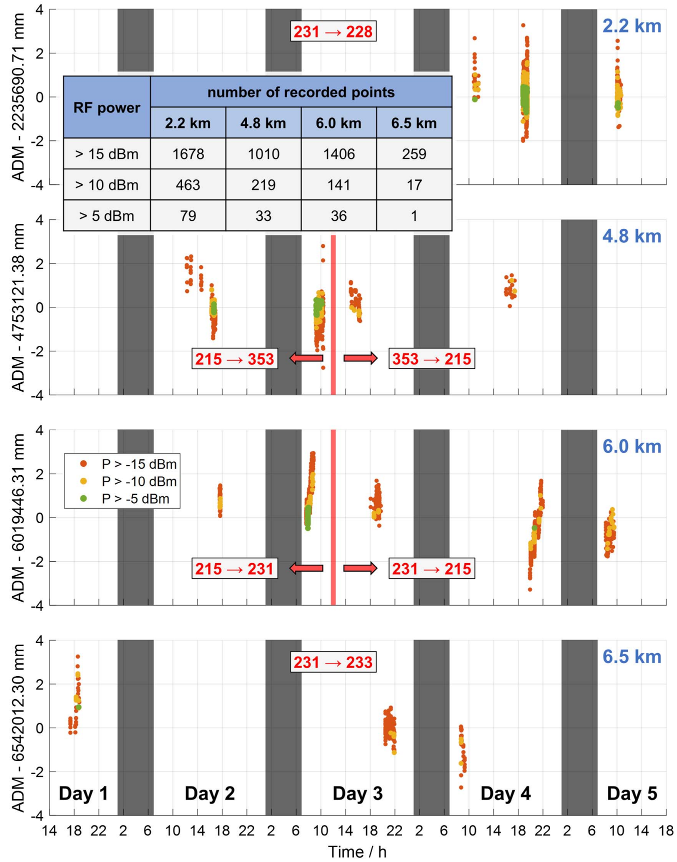

RF power	number of recorded points			
	2.2 km	4.8 km	6.0 km	6.5 km
> 15 dBm	1678	1010	1406	259
> 10 dBm	463	219	141	17
> 5 dBm	79	33	36	1

Fig. 3. Baseline lengths measured over 5 successive days for different received RF powers. The inset table summarizes the number of recorded points.

this measurement campaign, and the two optical beams are now perfectly aligned.

The four baselines were measured over several days, up to four for the baseline 231-215 of 6.0 km. This allows the number of points to be increased, and the long-term stability of the measurements to be verified. In addition, the baselines of 4.8 and 6.0 km were measured forward and backward, i.e., the positions of the instrument and the target were interchanged during the measurement campaign.

The measured baseline lengths are presented as a function of the time in Fig. 3. These curves are presented for different levels of received RF power: as will be seen subsequently, this is an important criterion for determining the uncertainties on L. In Fig. 3, distances are written in the form X → Y, with X corresponding to the pillar where the instrument was installed, and Y to the pillar where the target was mounted. The baselines of 4.8 and 6.0 km were measured from both sides (inversion at midday on Day 3). Day 1 is July 4, 2022, and the time axis corresponds to local time, i.e., greenwich mean time (GMT)+2.

The procedure for determining the distance values of the four baselines was as follows:

- Measurement of the optical path lengths D_1 and D_2. These are the two measurements carried out simultaneously by the ADM at two different wavelengths, at 780 nm for D_1 and at 1,560 nm for D_2. Each individual distance displayed in Fig. 3 is derived from measurements of phase difference $\Delta\phi_{\mathrm{RF}}(\lambda_i)$ [Eq. (4)] integrated over 20 ms.
- Selection of points with received RF powers above a certain level, ideally −5 dBm, for both wavelengths simultaneously. Fig. 3 shows that we have considered three cases: RF power higher than −15 dBm, higher than −10 dBm, and higher than −5 dBm. This corresponds to signal-to-crosstalk ratios of 50, 55, and 60 dB, respectively. Crosstalk, which is the dominant noise in the ADM, is explained in the next section.
- Correction of D_1 and D_2 from their instrument internal offsets to obtain the optical path lengths between the invariant points of rotation of the instrument and target gimbal mechanisms.
- Correction of D_1 and D_2 from the centering offsets of the instrument and target. These offsets result from the fact that the standing axes of the head and target are not aligned with the reference points of the pillars. These offsets were quantified prior to the measurement campaign in laboratory in a similar way to the characterization presented by Guillory et al. (2024), but with the forced-centering mount assembly that has been rotated inside a CERN socket.
- Calculation of the air-index compensated distance L using Eq. (1) and (2). The factor A was calculated using the Voronin and Zheltikov (2017) equation, which is well-adapted to the infrared wavelengths of the ADM. This formula was also used by Guillory et al. (2024) because it gives better results than using classical formulas. With this formula, the independence of the air-index compensated distance with air temperature and atmospheric pressure can be demonstrated in the same way as Eq. (3). However, in the Voronin and Zheltikov (2017) formula, humidity is expressed as a number density (number of water molecules per unit volume) and not as a partial pressure of water vapor.
- Geometrical reduction of L to determine the baseline length L_{baseline} between the reference points of the pillars. This is further explained in the "Geodetic Considerations" section.
- Plotting the histograms of the baseline lengths and fitting them with Gaussian distributions to determine their average value and standard deviation, as shown in Fig. 4. In the figure, each bar is

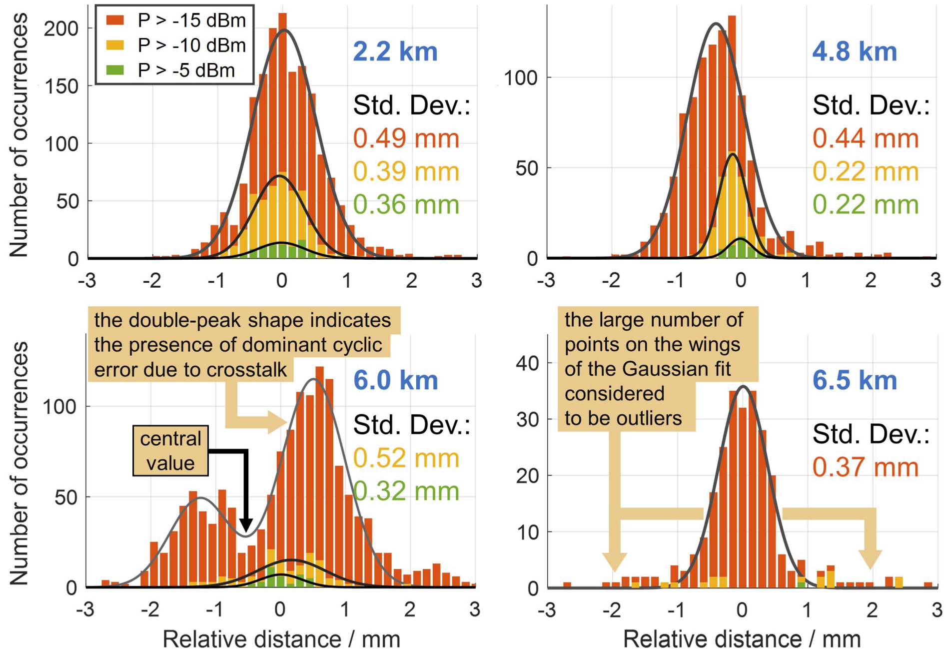

Fig. 4. Histograms of the baseline lengths obtained from Fig. 3, with the same indicators corresponding to the same levels of received power.

Table 1. Summary of the L_{baseline} measurements after Gaussian fit

Baseline	Power (dBm)	Average (mm)	Standard deviation (mm)
231→228	>−5	2,235,690.69	0.36
215↔353	>−5	4,753,121.35	0.18
231↔215	>−5	6,019,446.31	0.32
231→233	>−15	6,542,012.28	0.37

150 μm wide. When the number of recorded points is sufficient, a Gaussian fit was performed and the related standard deviation reported. For 6.0 km and RF powers higher than -15 dBm, the experimental histogram was fitted to a sum of two Gaussian curves due to the presence of a double peak. The results are summarized in Table 1. We could also have computed the average distance and the related standard deviation from the raw data, without performing a Gaussian fit. This choice was made because we know from previous research that the expected distributions should be Gaussian, and because such an approach smooths out the impact of potential outliers. In practice, the two approaches give almost identical results, except for the standard deviation of the 6.5-km baseline (the standard deviation on the raw data is twice higher because of a few outliers).

The measurements will be analyzed subsequently in the light of the estimated uncertainties and the results of the comparison with GBDM+ measurements ("Analysis" section). However, at first sight, the histograms in Fig. 4 show that the Gaussians fit the experimental measurements well. Moreover, the standard deviations of these Gaussians are less than half a millimeter. For measurements carried out over several days, and with reciprocal observations for the baselines of 4.8 and 6.0 km, this shows an excellent stability of the measurements, reflecting among other things the good compensation of the air refractive index for air temperatures varying between 15°C and 32°C and atmospheric pressures (around 960 hPa) varying by about 10 hPa for a given location. In practice, an operator who intends to measure baselines of several kilometers will not necessarily carry out measurements over several days. As soon as a return RF signal higher than -5 dBm is obtained, which is recommended to minimize the uncertainty ("Uncertainty of the Baseline Lengths" section), the measurement is considered valid. In this case, whatever the measurement of RF power higher than -5 dBm is chosen from all the measurements recorded, the result obtained will not differ by more than 1 mm from the average values given in Table 1.

Uncertainty of the Baseline Lengths

The uncertainty of the air-index compensated distance can be calculated through the relationship presented in Eq. (1). To this end, we have to propagate the uncertainties in the input variables, i.e., the optical path lengths D_i and the factor A. As demonstrated by Guillory et al. (2024), for a factor A significantly higher than one and treated it as if were error-free, the uncertainty in L is

$$\begin{aligned} u(L)^2 &= u(D_1)^2 + A^2 \times u(D_2 - D_1)^2 - 2A \times \mathrm{cov}(D_1; D_2 - D_1) \\ &\simeq A^2 \times u(D_2 - D_1)^2 \quad \text{for } A \gg 1 \end{aligned} \tag{5}$$

The remainder of this section is organized as follows. In the "Two-Wavelength ADM" section, we recall some of the results presented by Guillory et al. (2024), then we calculate the uncertainties in the optical path lengths D_1 and $D_2 - D_1$ for the specific case of the CERN measurement campaign. In "Air-Index Compensated Formula and the Humidity Content" section, the impact of the factor A is discussed. In the "Geodetic Considerations" section, the uncertainties due to the geometric corrections used to pass from the air-index compensated distances L to the baseline lengths L_{baseline} are assessed, considering an ellipsoidal Earth model. Finally, in the "Summary" section, the results are summarized and discussed.

Two-Wavelength ADM

The uncertainty of the ADM has been assessed by Guillory et al. (2024), and it is equal to 323 μm ($k = 1$) under favorable experimental conditions. However, these conditions can be difficult to

J. Surv. Eng., 2025, 151(1): 04024014

achieve in the field when measuring distances of several kilometers. Indeed, a poor atmospheric visibility leads to the deterioration of the signal-to-noise ratio, with crosstalk as the dominant noise. The latter is a spurious signal that adds to the measurement signal and induces a cyclic error as a function of the measured distance, with a period of about 29.6 mm. It can be caused by leakages from the RF synthesizer to the ADM reception stages or back reflection in optical components. Experimental conditions are considered favorable if the signal-to-crosstalk ratio (SCR) is higher than 60 dB at each wavelength, which is the case when the received RF powers are higher than −5 dBm (Figs. 3 and 4). If they are lower, the performance of the ADM is degraded, with, for example, an uncertainty in the air-index compensated distance of 752 μm ($k = 1$) for SCR of 50 dB for both wavelengths.

It should be underlined that the important term in Eq. (1) is the difference of optical path lengths $D_2 - D_1$ because any error on this difference is multiplied by a factor A of 48. This term is mainly impacted by the cyclic errors present at each wavelength and due to crosstalk. The difference between these cyclic errors depends on the difference between their phase, $\Delta\phi_{CE}$. Guillory et al. (2024) showed that this phase shift is a function of the measured optical path lengths: at some distances these cyclic errors cancel out, whereas at other distances, they add up

$$\Delta\phi_{CE}(L, T, p, x, p_\omega) = \phi_{CE}(D_2) - \phi_{CE}(D_1) = \Delta\phi_{CE}(L = 0) + 4\pi \times \Delta n(T, p, x, p_\omega) \times L \times \frac{f_{RF}}{c} \tag{6}$$

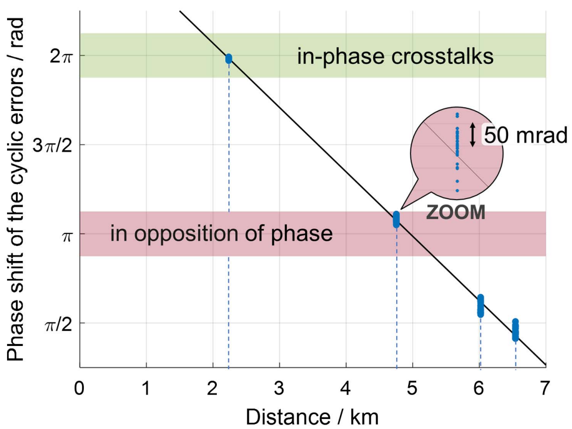

Fig. 5. Phase shifts $\Delta\phi_{CE}$ between the cyclic errors of the two wavelengths determined from Eq. (6). The observed variations at a given distance are due to changes in the weather conditions during the measurement campaign.

where $\Delta\phi_{CE}(L = 0)$ = phase difference of the cyclic errors measured for distance zero, i.e., 1.2 π in our case; and Δn = difference in refractive indices between the two wavelengths, where Δn depends on the environmental parameters and equals to about 5.35×10^{-6} for the weather conditions of the CERN measurement campaign.

Fig. 5 shows the phase shift $\Delta\phi_{CE}$ for the four baselines that have been measured. The distance of 2.2 km is a favorable case where the cyclic errors on D_2 and D_1 cancel out when calculating the air-index compensated distance, whereas for the distance of 4.8 km, they add up.

The two uncertainty values stated above for $k = 1$, namely, 323 and 752 μm for SCRs of 60 and 50 dB, respectively, assumed the measurement of a random distance where all possible values of $\Delta\phi_{CE}$ are considered, from 0 to 2π, and uniformly distributed. This is a general case. However, from Fig. 5, an uncertainty specific to each measured distance can be provided.

For this purpose, we consider a SCR of 60 dB for the baselines of 2.2, 4.8, and 6.0 km, and SCR of 50 dB for the baseline of 6.5 km. Indeed, for the longest distance, the number of points whose RF power level is above −10 dB m is too low, as shown in Fig. 3. The amplitudes of the cyclic errors on D_2 and D_1 are then deduced, 4.7 μm when the SCR is equal to 60 dB and 14.9 μm when it is equal 50 dB.

Next, the amplitudes of the resulting cyclic errors in the difference of optical path lengths $D_2 - D_1$ are determined using the phase shift values in Fig. 5: amplitudes of 0.2, 9.3, 7.7, and 19.8 μm for, respectively, baselines of 2.2, 4.8, 6.0, and 6.5 km. Due to the factor A of 48 in Eq. (1), the crosstalk therefore induces errors in the air-index compensated distance up to 950 μm. However, we cannot correct theses errors, only quantify their amplitude for uncertainty assessment, because we do not know where these errors lie in their cycle of about 29.6 mm period (this depends on the environmental parameters).

Other sources of error must also be taken into account, but crosstalk remains the main component. This is detailed by Guillory et al. (2024) and summarized in Table 2. Finally, the uncertainties ($k = 1$) in the difference of optical path lengths in Eq. (1), i.e., in $D_2 - D_1$, are equal to 4.1, 7.8, 6.8, and 14.6 μm for, respectively, baselines of 2.2, 4.8, 6.0, and 6.5 km.

Regarding the uncertainty on the first component of Eq. (1), i.e., D_1, it is about 55 μm ($k = 1$). This value includes the corrections from the instrument offset and the centering offsets. All the details have been given by Guillory et al. (2024).

Air-Index Compensated Formula and the Humidity Content

The calculation of the air-index compensated distance in Eq. (1) is based on the factor A, and by extension on the Voronin and Zheltikov (2017) equation. No associated uncertainty has been stated for this

Table 2. Uncertainty budget for the difference of optical path lengths $D_2 - D_1$

Uncertainty component	Source of uncertainty	Comment	Distribution	Uncertainty contribution ($k = 1$)
$u_{f_{RF}}$	Values of the RF modulation	$D_2 - D_1 \sim 5.35 \times 10^{-6} L$	Uniform	$4.8 \times 10^{-10} (D_2 - D_1)/(2 \times \sqrt{3})$
$u_{crosstalk}$	Presence of crosstalk at each wavelength	SCR from 50 to 60 dB	Arcsine	Up to $19.8/\sqrt{2}$ μm
$u_{AM/PM}$	Amplitude to phase coupling at the photodetection	The errors that occur at each wavelength are independent contributions	Uniform	0.9 μm
u_{random}	Random noise on the phase measurement	Value measured by Guillory et al. (2024)	Normal	1.6 μm
u_{offset}	Difference of instrument offsets between the two wavelengths	u_{offset} and $u_{long\text{-}term\ drift}$ were determined simultaneously in a single experiment.	Normal	3.7 μm
$u_{long\text{-}term\ drift}$	Long-term effects (drifts due, for example, to thermal expansion)	Only one of these contributions is considered in the MC simulation.	Normal	3.7 μm

equation, but we can give a few orders of magnitude for the factor A, which is a multiplicative factor of the difference of optical path lengths $D_2 - D_1$. Under the atmospheric conditions of the CERN campaign, $D_2 - D_1$ evolved at a rate of about −5.35 mm per km. For example, this difference is equal to -34.8 ± 0.2 mm for the baseline of 6.5 km. In this case, if the factor A varies by 6×10^{-4}, then an error of 1 mm is induced on the air-index compensated distance. According to Eq. (2), such a requirement means that the error on the dispersion terms $K(\lambda_i)$ must be less than 13 ppm. The knowledge of the factor A is obviously less demanding for short distances.

The air-index compensated distance does not depend directly on the temperature and pressure, but only on the humidity of the air, which is expressed as a number density N_{H2O} in the Voronin and Zheltikov (2017) equation. It was determined from weather stations as follows:

$$N_{\mathrm{H2O}} = \frac{p_\omega}{k_B T} = \frac{1}{k_B T} \times \frac{\mathrm{RH}}{100} \times p_{\mathrm{sat}}(T) \tag{7}$$

where p_w = partial pressure of water vapor (Pa); k_B = Boltzmann constant; T = temperature (K); RH = relative humidity (which lies between 0 and 100); and p_{sat} = saturation water vapor pressure (Pa).

In practice, we used standard hygrometers that measure humidity in the form of a relative humidity, and we coupled this value with a temperature measurement T made by the same sensor. These parameters were measured at the instrument location with a Vaisala PTU300 (Vaisala Oyj, Vantaa, Finland) and at the target location with a Fluke 971 (Fluke Corporation, Everett, Washington). These sensors provide, respectively, relative humidity at ±1% and ±2.5%, and temperature at ±0.2 K and ±0.5 K. Both RH and T varied considerably during the measurement campaign, but the humidity appeared more stable when expressed as a number density $N_{\mathrm{H2\,O}}$. On Day 1, the number of molecules per cubic centimeter was mainly between 380×10^{15} and 420×10^{15}, then from Day 2 to Day 5, it varied between 250×10^{15} and 330×10^{15}.

Under the atmospheric conditions of the measurement campaign, the number density measured at the instrument location was known with an uncertainty better than 10×10^{15} molecules per cubic centimeter ($k = 1$), and that measured at the target location with an uncertainty better than 25×10^{15} molecules per cubic centimeter ($k = 1$). These values were obtained for RH = 55% and $T = 27$°C, which corresponds to typical values of the first day, i.e., when the atmospheric conditions induced the higher uncertainty in N_{H2O}. Considering these uncertainty values, the number densities measured at both sides of the baselines were compatible, regardless of the pillars chosen. Thus, for the calculation of the air-index compensated distance, we used the humidity measured at the instrument side because its value was recorded continuously, and we considered an uncertainty of 10×10^{15} molecules per cubic centimeter ($k = 1$).

By injecting the uncertainties in N_{H2O} estimated previously into the equation of the air-index compensated distance, the contribution of humidity to the distance uncertainty depends on the distance and is equal to 30.2 μm/km, i.e., 68 μm at 2.2 km and 198 μm at 6.5 km ($k = 1$).

Geodetic Considerations

The ADM distances from the center of instrument to the center of target have to be reduced to the reference points of the pillars (an example is depicted in Fig. 6 for the baseline 215−353 of 4.8 km). The head and target having been leveled and their centering offsets corrected, their center is considered to be above the reference points of the pillars (i.e., along the standing axes of the head and target). Taking into account that this reduction, which is a potential source of error to be avoided, must be determined with an uncertainty below 1/10 of a millimeter and facilitate straightforward uncertainty propagation, neither the standard approach based on local Cartesian coordinates normally used in length metrology, nor the traditional geodetic approach based on geodesic lines are suitable. For the sake of smooth reading, the mathematical expressions used in this experiment, which are based on known geodetic coordinates of pillars, their ellipsoidal heights, and the instrument offsets as well as their corresponding errors, are detailed in Appendix I. This formulation is common for the correction of heights in the three different measurement techniques (ADM, GBDM+, and EDM).

The heights of the instrument and the target were determined for each pillar, with the upper edge of the bore of the CERN socket as reference [Fig. 7(g)]. In the field, the reference heights were determined using a 88.9 mm (3.5 in.) sphere whose center is defined by a circular pattern target [Fig. 7(a)]. The offset between the center of such a sphere and the upper edge of the bore was then provided by CERN to the nearest 0.1 mm [Fig. 7(b)]. Next, for Pillars 215, 231 and 353, the heights of the ADM and its target were measured by IGN using a total station (Leica TM50 0.5) and 38.1 mm (1.5-in.) retroreflective targets placed in nests [Figs. 2 and 7(a)].

Some of these targets were used as fixed points to link the optical measurements of the first week of the campaign with the GNSS measurements of the second week. Other targets materialize the heights of the transit axes of the gimbal mechanisms with an uncertainty of 0.2 mm ($k = 1$), from which the heights of the optical beam are derived. Guillory et al. (2024) determined the positions of the optical beam with respect to the transit axes to

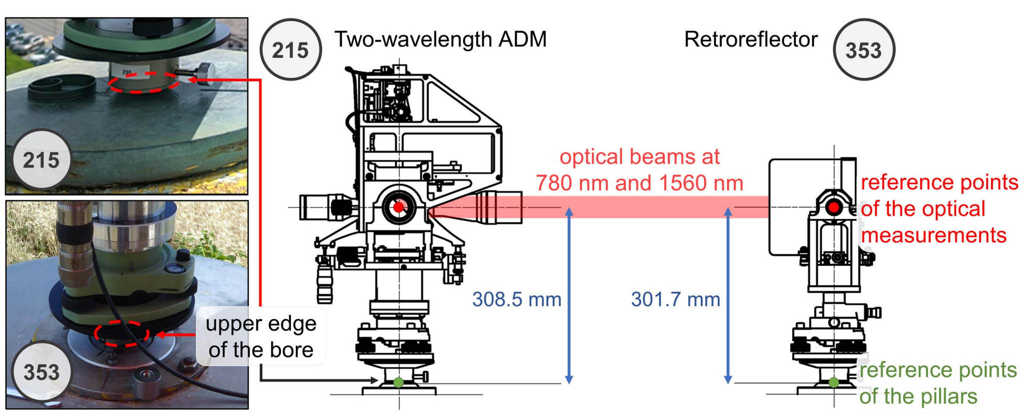

Fig. 6. Example of the baseline 215–353 of 4.8 km with the optical head on pillar 215 and the target on pillar 353.

J. Surv. Eng., 2025, 151(1): 04024014

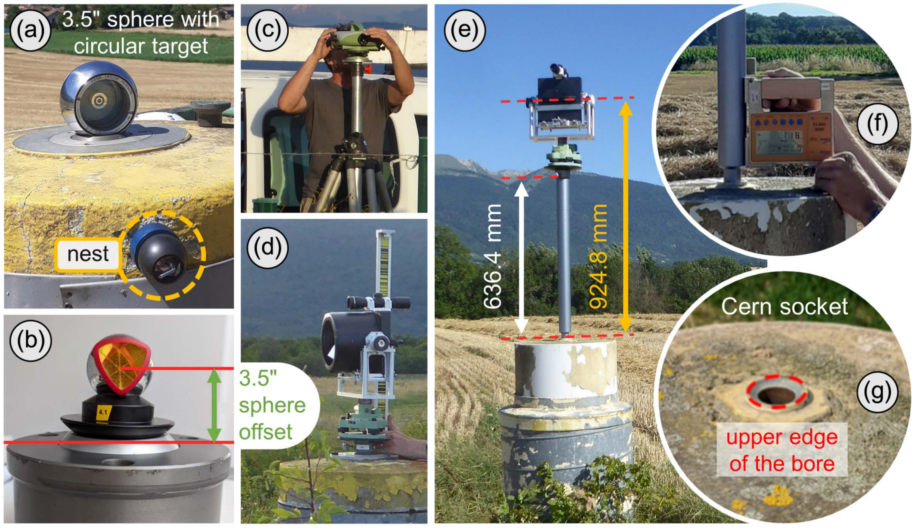

Fig. 7. Height measurements of the instrument and the target with respect to the upper edge of the bore of the CERN socket, which is depicted in plot (g): (a) height measurement of a 88.9 mm (3.5-in.) sphere at Pillar 231; (b) offset measurement of such a sphere in laboratory; (c and d) height measurement of the target at Pillar 233 for the 6.5 km baseline; and (e–g) height measurement of the target at Pillar 228 for 2.2 km baseline.

be 1.07 and 0.05 mm above these axes for, respectively, the head and the target. To this value, we have added the uncertainty of the measurement of heights at the total station, estimated at 0.4 mm ($k = 1$).

For Pillars 228 and 233, the heights were determined by a different method, using a digital level (Leica DNA03) and an invar leveling staff [Fig. 7(c)]. In this case, the uncertainty in the positioning of the leveling staff [Fig. 7(d)] with respect to the optical beam was estimated to be 0.1 mm ($k = 1$), and the uncertainty in the measurements of heights with this technique was estimated to be 0.1 mm ($k = 1$). In the end, we have assumed that the combined uncertainty of the heights [positioning of targets or leveling staff, height measurements, and 88.9 mm (3.5-in.) sphere offset] is 0.45 mm ($k = 1$) for Pillars 215, 231, and 353, and 0.25 mm ($k = 1$) for Pillars 228 and 233.

For the baseline of 2.2 km, in order to make the target visible from the instrument, an extension of 636.4 mm was added on Pillar 228, i.e., on the target side [Fig. 7(e)]. This value is derived from two successive measurements of a 88.9 mm (3.5-in.) sphere with the digital level, first when the sphere is placed on the extension socket, then when it is placed on the pillar socket. Because the diameter of the upper edge of the bore of the extension socket has not been accurately measured and may be slightly different from that of the pillar socket, an uncertainty of 1 mm ($k = 1$) was assumed for the extension length.

Additional corrections were applied to the measured distance due to the leveling of this extension. The errors of verticality were measured using a Wyler Clino 2000 inclinometer (Wyler AG, Winterthur, Switzerland) [Fig. 7(f)], with angular errors of less than 30 arcseconds (approximately 145 μm/m, or when this error limit is converted into an uncertainty value, assuming a uniform error distribution, 84 μm/m at $k = 1$): there are 3.1 mrad in the direction of the aiming line and 0.6 mrad in the direction perpendicular to the baseline. These reduce the measured distance by 2.1 mm and add 0.4 mm to the right of the aiming direction. We assumed that these additional geometric corrections contribute to the uncertainty of the baseline lengths by 0.05 mm ($k = 1$). However, the evolution over time of vertical extension, due for example to bending under the effect of incident solar radiation, has not been verified.

In the end, reducing the air-index compensated distances L of 4.8, 6.0, and 6.5 km to baseline lengths L_{baseline} decreased the measured values by 80–220 μm. For the baseline of 2.2 km, its length was 13.03 mm larger than that measured optically due to the use of the extension. In any case, this distance reduction contributes to the uncertainty of the baseline lengths L_{baseline} up to 60 μm.

Summary

In order to determine the uncertainty in the baseline lengths measured by the Cnam two-wavelength ADM, six uncertainty components have been considered: u_{D1}, u_{D2-D1}, u_{N_H2O}, $u_{K(\lambda i)}$, $u_{g(\lambda i)}$, and $u_{\mathrm{geometric}}$. Their values are reported in the first lines of Table 3. So far, the uncertainties in the dispersion terms $K(\lambda_i)$ and humidity terms $g(\lambda_i)$ have not been estimated. Consequently, the uncertainty in the baseline lengths L_{baseline} is optimistic. It is therefore an

Table 3. Summary of the uncertainties for the air-index compensated distance L

Uncertainty component	Uncertainty ($k = 1$) 2.0 km	4.8 km	6.0 km	6.5 km	Uncertainty contribution to L_{baseline} ($k = 1$)
u_{D1} (μm)	54.8	54.8	54.8	55.8	About 55
u_{D2-D1} (μm)	4.1	14.6	6.8	14.6	Up to 48.05×14.6
u_{N_H2O}	10×10^{15} molecules per cm^3				30.2 parts per billion (ppb)
$u_{K(\lambda_i)}$ and $u_{g(\lambda_i)}$	Unknown, it must be determined in the future, e.g., by refractometry				$u_A \times 5.35$ ppm, with u_A unknown
$u_{\mathrm{geometric}}$ (μm)	60	6	5	17	Up to 60
u_{L_baseline} (μm)	225	403	376	723	—

instrumental uncertainty, taking into account the measurements of distance and humidity.

In the current study, the physical model has been treated as if it were without error because the formula for the refractive index of air proposed by Voronin and Zheltikov (2017) has no associated uncertainty. As shown in the "Air-Index Compensated Formula and the Humidity Content" section, the factor A of about 48 must however be known to better than 6×10^{-4} for the largest distance of 6.5 km if we do not want to induce an additional error of 1 mm. Ultimately, such a requirement on the factor A requires knowledge of the dispersion terms $K(\lambda)$ at better than 13 ppm.

Finally, the uncertainties in the baseline lengths were calculated as the sum of the squared standard uncertainty contributions. This combined uncertainty is reported in the last line of Table 3.

GBDM+ Method

Principle

A possible alternative for the absolute determination of outdoor distances with uncertainties of 1 mm or better is the use of GNSS. We follow here the improved methodology for a GNSS-based distance meter (GBDM+) that was presented by Baselga et al. (2022) as an improvement over the work of García-Asenjo et al. (2021). As explained therein, the use of GNSS in metrology is appealing for several reasons: the scale of these systems is consistent with the definition of the SI meter—given its maintenance through the use of atomic clocks—and has proven to be globally stable at the 0.001 ppm level; besides, currently available GNSS receivers and antennas make it possible to obtain measurements with noise on the order of 1 mm or lower. However, there are difficulties in rigorously obtaining the total uncertainty in the measured distance as the result of the individual uncertainties of all the contributing sources. The GBDM+ approach tries to overcome this difficulty.

As presented by Baselga et al. (2022), the GBDM+ approach follows the strategy of (1) estimating the corrections of all contributing error sources along with their corresponding uncertainties at the level of zero differences in the GNSS processing, (2) propagating the uncertainties to the double differences and (3) propagating the uncertainties to the final determination of the distance after the least-squares adjustment of the double-difference equations.

For the GNSS processing, we use additional GNSS standard products:

- SP3 and CLK files as provided by the International GNSS Service (IGS) (Johnston et al. 2017) for satellite orbits and final clocks, respectively.
- ANTEX files as provided by the IGS for constants and variations in satellite antenna phase centers.
- ANTEX files of generic and individual calibrations for receiver antenna phase center offsets and variations.

A precise point positioning (PPP) with CSRS-PPP (Banville et al. 2021) permits us to obtain station coordinates and their corresponding uncertainties, tropospheric delays and their corresponding uncertainties, receiver clock offsets and their uncertainties, and carrier phase residuals. In its current version (version 3), the CSRS-PPP service estimates ionospheric delays but does not distribute them to the users; this output may be added shortly as part of the forthcoming version 4 (S. Banville, personal communication, 2021). In any case, the iono-free combination L3, which is free of ionospheric effect to first order, cancels out the effect for all practical purposes after double differencing. With the sidereal filtering technique over the carrier phase residuals (Baselga et al. 2022; García-Asenjo et al. 2021), the multipath can be corrected to first order of magnitude and the corresponding uncertainty estimated. In the case of antenna phase center offset and variations, the value from the individual calibration is used as correction, and its difference with respect to the one for the general calibration is used in absolute value as the uncertainty ($k = 1$) in the correction.

The GBDM+ functional model of double-differenced corrected carrier phases (Baselga et al. 2022) then permits obtaining the baseline distance along with its uncertainty rigorously propagated from all significant error sources.

Measurement of the Baseline Lengths

Five Leica GR25 GNSS receivers along with five individually calibrated Leica AR25 choke ring antennas were used to observe satellites in the four global constellations (GPS, Galileo, GLONASS, and BeiDou) with a sampling rate of 1 s.

The setup at each station included a protected meteorological sensor in order to study in the future the advantages of a possible improved tropospheric modeling (Fig. 8).

The antenna height on each pillar was accurately measured by IGN using a total station and the same procedure as for the ADM the previous week, as shown in Fig. 9.

The GNSS observations were collected from July 11, 2022, at 9:57 GMT to July 14, 2022, at 19:05 GMT, resulting in between 2 days 22.5 h and 3 days 3.0 h of useable data for the different GNSS stations. After the due processing by means of the GBDM+ method, they give rise to the baseline lengths and corresponding uncertainties shown in the next section.

Uncertainty of the Baseline Lengths

As explained, all contributing error sources in the double-differenced carrier phase equations are estimated first at the zero-difference level, then propagated to the double-difference level and then, through the least-squares algorithm to the final baseline distance.

Fig. 8. Example of the GNSS setup on a pillar.

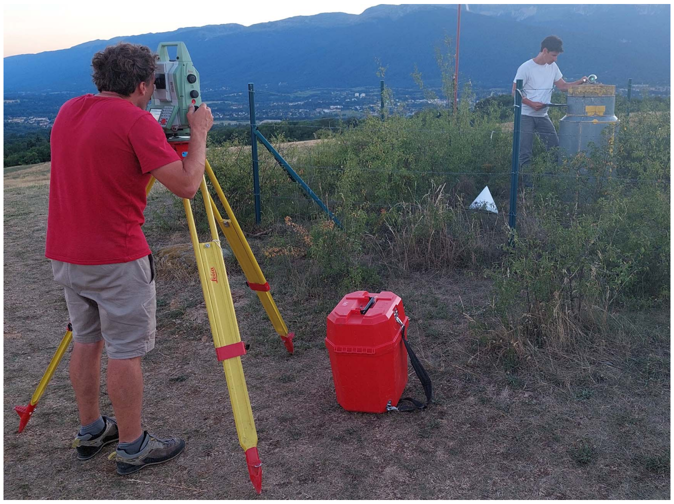

Fig. 9. Determining antenna height above pillar by Total Station.

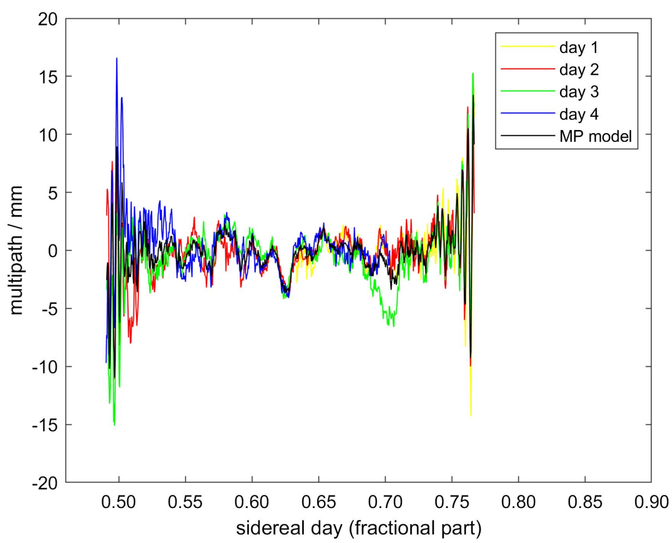

Fig. 10. Multipath correction model for Satellite G04 and Station P231.

At the zero-difference level, the corrections applied and corresponding uncertainties considered include receiver clocks (by PPP, with negligible uncertainties after the double differencing), multipath (by PPP residuals and sidereal filtering), tropospheric delay (by PPP), and antenna correction (by individual and generic absolute antenna calibrations).

As an example of the corrections at the zero-difference level we show in Fig. 10 the multipath correction for Station 231 (used in the baselines of 2.2, 6.0, and 6.5 km) and satellite G04 obtained after the sidereal matching.

The estimated uncertainties at the level of zero differences are propagated to the double-difference equations for each of the contributing sources of error. Then, the corresponding uncertainty in each error source propagates to the final baseline length through the equations of the least-squares model. Besides, the geometrical reduction from antenna centers to pillar references, along with the corresponding uncertainty, was also taken into account. It would also be possible to include in the uncertainty budget an estimate of the monument stability estimation, but we have not attempted to do so in the present case due to insufficient information about the behavior of every pillar. Table 4 presents the uncertainties for every contributing source in the baseline 231-233.

Table 4. Uncertainties in contributing sources for baseline 231-233

Error source	Uncertainty at $k = 1$ (mm)
Tropospheric delay	0.29
Multipath	0.14
Antenna calibration	0.20
Antenna height	0.02
Total	0.38

Table 5. Summary of GBDM+ results

Baseline	Value (mm)	Uncertainty at $k = 1$ (mm)
231–228	2,235,691.07	0.32
215–353	4,753,123.72	0.32
231–215	6,019,445.93	0.42
231–233	6,542,012.96	0.38

Finally, the baseline lengths and corresponding uncertainties for the four baselines determined by the GBDM+ approach are given in Table 5.

Single-Wavelength EDM: Mekometer ME5000

The comparison GBDM+ versus classical EDM (Kern Mekometer ME5000 operating at 632.8 nm) was presented by García-Asenjo et al. (2022). The results are not fully illuminating for two main reasons: first, the two baselines whose lengths exceed 5 km are out of the range of the EDM and could not be measured, and second, the two shortest baselines of 2.2 and 4.8 km have a high uncertainty due to the first velocity correction. The air refractive index along the optical beam path was derived from meteorological sensors installed in the baseline endpoints only. As a result, its value is hard to determine with an uncertainty better than 1 ppm, which would correspond to an uncertainty of better than 1 K on the temperature seen by the beam over several kilometers. We did not attempt to estimate the uncertainties, but the experimental deviations of the measured distances are already higher than the desired 1 mm ($k = 2$). The comparison of the different techniques, including the EDM, highlights the advantages of the instruments developed, ADM and GBDM+.

The distances and experimental deviations resulting from the EDM, after calibration and consideration of geometrical and meteorological corrections, are 2,235.6934 m $\pm$ 1.3 mm ($k = 2$) and 4,753.1223 m $\pm$ 1.7 mm ($k = 2$).

Two-Wavelength ADM versus GBDM+

Comparison

For the comparison measurements between the ADM and the GBDM+, we define reference values of the baselines, L_{ref}, and the related standard uncertainties, u_{ref}, as follows (Beissner 2002):

$$L_{\mathrm{ref}} = \frac{p_1 \times L_1 + p_2 \times L_2}{p_1 + p_2} \tag{8}$$

$$u_{\mathrm{ref}} = \frac{\sqrt{(p_1 \times u_1)^2 + (p_2 \times u_2)^2}}{p_1 + p_2} \tag{9}$$

where L_i and u_i = distances and standard uncertainties of the measurements performed by the GBDM+ for $i = 1$ and by the ADM for $i = 2$. As for the weights p_i, they are equal to the inverse of the variances

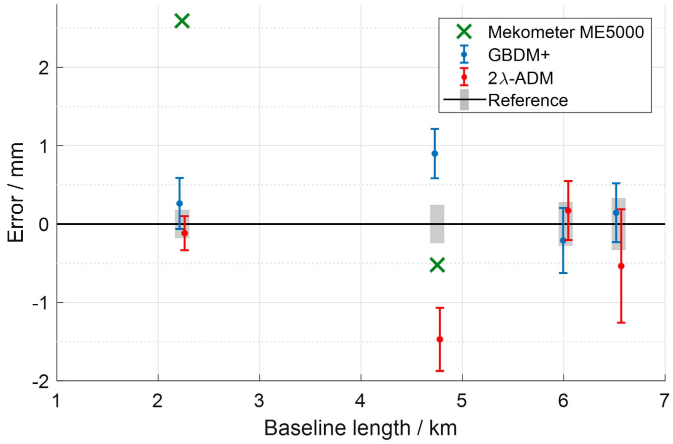

Fig. 11. Errors observed on the measurements performed by the GBDM+ and the ADM relatively to the reference value. The uncertainty bars correspond to a coverage factor k of 1. The values obtained by the Mekometer ME5000 are also given for comparison.

$$p_i = \frac{1}{u_i^2} \tag{10}$$

This results in the comparison shown in Fig. 11.

Analysis

Analysis for 2.2 km

For the ADM measurements, the atmospheric visibility was high, the optical losses due to air propagation over this short distance were low, and consequently the SCRs were high. In addition, the system was insensitive to crosstalk because the cyclic errors of the two wavelengths cancelled each other out as shown in Fig. 5. Therefore, the Gaussian model fit the experimental data well, and this for the different levels of received power. Finally, the differences observed with the GBDM+ measurements were less than half a millimeter, -0.43 mm for a SCR of 60 dB, and the values estimated by the two techniques were compatible within the calculated uncertainties at $k = 1$, as shown in Fig. 11.

The distance measured by the single-wavelength EDM was 2.3–2.7 mm larger than those measured by the ADM and the GBDM+. This error can be explained, for example, by an overestimation of the temperature seen by the optical beam by about 1.2 K, and therefore an air refractive index lower than it is. Indeed, the temperature used in the calculation of the air refractive index contributes to the measured distance by -0.95 ppm/K.

Analysis for 4.8 km

As shown in Fig. 5, the ADM was highly sensitive to crosstalk as the cyclic errors of each measured optical path length added up. However, the histograms corresponding to this measurement, in Fig. 4, are not those expected, i.e., a distribution typical of the presence of a cyclic error, characterized by a double-peak shape. This is probably because the phase of the cyclic error is not uniformly distributed between zero and 2π. The distributions were rather close to Gaussian distributions, with central values that tended toward a value free of the cyclic error as the SCR improved. For an SCR of 60 dB, the maximum expected error due to crosstalk, i.e., the amplitude of the cyclic error, was 0.45 mm. Nevertheless, the difference observed with the GBDM+ measurement was much larger than expected, i.e., -2.32 mm for a SCR of 60 dB, as shown in Fig. 11.

As stated by García-Asenjo et al. (2022), the GBDM+ processing of this baseline was a bit problematic with results depending on the processing time more than expected. A possible explanation could be that there were systematic errors not fully compensated for that affected the result obtained after the weighted average of time blocks. Another explanation could be that Pillar 215, one of the baseline endpoints, is on top of a building and therefore more subject to possible movements (dilations, tilting, and so on) than the others and thus not able to guarantee submillimetric stability along the course of all measurements.

The results of the measurement with the Mekometer ME5000, although not reliable in terms of accuracy, fall in between those of the ADM and GBDM+.

Analysis for 6.0 km

For a SCR of 60 dB, the difference observed between the ADM and GBDM+ measurements was 0.41 mm. Despite the poor number of recorded points, the result is as good as the one obtained at 2.2 km. In addition, the values estimated by the two techniques were compatible within the calculated uncertainties at $k = 1$, as shown in Fig. 11.

It is also interesting to observe the histogram in Fig. 4 for RF powers down to -15 dB m, and thus for crosstalk that dominates the other noises. The crosstalk leads to a cyclic error (of arcsine distribution), which in practice results in a histogram with a double-peak shape: it is not completely symmetric because some phases of the cyclic error are more present than others. It was therefore fitted to a sum of two Gaussian curves: the central value of this fit, which in theory tends toward the true value, differed from the GBDM+ measurement by only 0.14 mm.

Analysis for 6.5 km

The number of points recorded with the ADM was low due to the high optical losses when propagating through the air over such a long distance. As a result, we have retained only the measurements with RF powers down to -15 dB m, i.e., SCRs of 50 dB. However, the difference between the two measurement systems was only 0.70 mm, and their estimated values were compatible within the calculated uncertainties at $k = 1$, as shown in Fig. 11.

We have recorded a single point with a RF power higher than -5 dBm and therefore a SCR better than 60 dB. This is not enough to make a statistical analysis or a Gaussian fit, but it should be underlined that this single measurement differs from the GBDM+ by only 0.25 mm. This value has an uncertainty of 0.34 mm.

Conclusion

The instrumental uncertainty of the two-wavelength ADM, which was studied in a previous paper, has been recalculated in the current paper for the specific distances of the four baselines from 2.2 to 6.5 km measured in the CERN geodetic network. For a full assessment of the uncertainty, it is necessary to take into account the uncertainty of the model used to switch from a measurement of two optical path lengths to a measurement of air-index compensated distance. Currently, this is not the case, and we have yet to determine the uncertainty of the A factor, or more specifically of the dispersion and humidity terms, $K(\lambda)$ and $g(\lambda)$, which in our case are derived from the Voronin and Zheltikov (2017) equation. On the other hand, the GBDM+ technique, previously tested in shorter calibration baselines, has been optimized for distances up to 6.5 km and externally validated at submillimetric level by using the ADM developed by Cnam in the well-controlled CERN geodetic network.

In the absence of the uncertainty values for the dispersion and humidity terms, the comparison carried out in this article has also validated the use of the Voronin and Zheltikov (2017) equation because the difference with the GBDM+ technique was less than

0.7 mm for three of the four distances measured. For the fourth distance of 4.8 km, which was measured by the ADM over several days and from both sides, it showed a difference of 2.7 mm with the GBDM+ measurement. Further investigations are required to understand this discrepancy. However, the reproducibility of this distance measurement, regardless of the side from which the measurement is performed, and the long-term stability, are good indicators of the accuracy of this measurement.

In the long term, Cnam plans to carry out refractometry measurements at 780 and 1,560 nm in order to define its own dispersion values and attribute an uncertainty value to these quantities. In the nearer future, a new joint observation campaign is being planned by Cnam, UPV, and CERN to perform additional measurements over a larger number of distances, which will hopefully confirm the validity of these results.

Appendix I. Reduction of the Slope Distances to the Pillar Reference Points in an Ellipsoidal Earth

We provide here a detailed description of the procedure to rigorously reduce the slope distances measured in the field from the center of the instruments to the height reference points of the pillars (s', t') to (s, t), respectively, in Fig. 12.

Although the geometric reduction process is normally based on coordinates referred to a local Cartesian system, which entails that verticals are considered parallel, when the aimed accuracy is of the order of 10^{-7} at several kilometers, the Earth's curvature has to be taken into consideration. By introducing a proper geodetic reference system, for example, the ETRS89, whose ellipsoid of reference is the GRS80, the geodetic coordinates (φ, λ)—which define the orientation of the geodetic vertical—along with the ellipsoidal height h fully define the three-dimensional (3D) position of a point with regard to an ellipsoidal Earth. Nevertheless, the determination of the geometric correction and its uncertainty is largely simplified by using the so-called Earth-centered Earth-fixed coordinates (ECEF) instead of the original triplet (φ, λ, h).

The ECEF coordinates (X, Y, Z) are unambiguously related to the geodetic ones by the following equations:

$$X = (\nu + h)\cos\varphi\cos\lambda \tag{11}$$

$$Y = (\nu + h)\cos\varphi\sin\lambda \tag{12}$$

$$Z = [\nu(1 - e^2) + h]\sin\varphi \tag{13}$$

where $\nu = a(1 - e^2\sin^2\varphi)^{-1/2}$ is the Earth's prime-vertical radius of curvature; and e = eccentricity of the ellipsoid.

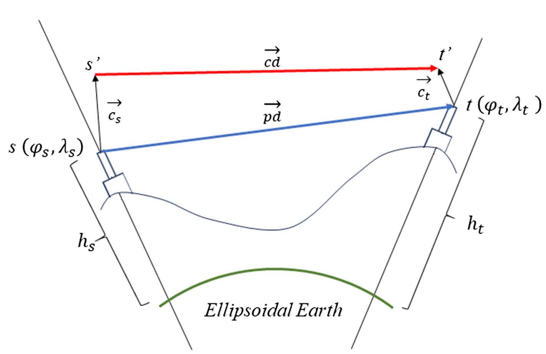

Fig. 12. Scheme for consideration of the rigorous reduction of instrument heights in an ellipsoidal Earth.

Therefore, the components of the vector $\overrightarrow{pd}$ connecting the geodetic marks s and t in the ECEF system are

$$\Delta X_{st} = (\nu_t + h_t)\cos\varphi_t\cos\lambda_t - (\nu_s + h_s)\cos\varphi_s\cos\lambda_s \tag{14}$$

$$\Delta Y_{st} = (\nu_t + h_t)\cos\varphi_t\sin\lambda_t - (\nu_s + h_s)\cos\varphi_s\sin\lambda_s \tag{15}$$

$$\Delta Z_{st} = [\nu_t(1 - e^2) + h_t]\sin\varphi_t - [\nu_s(1 - e^2) + h_s]\sin\varphi_s \tag{16}$$

On the other hand, the centers of instruments, s' and t' are related to the geodetic marks (mechanical points of reference) s and t by

$$\begin{pmatrix} X_{s'} \\ Y_{s'} \\ Z_{s'} \end{pmatrix} = \begin{pmatrix} X_s \\ Y_s \\ Z_s \end{pmatrix} + R(\varphi_s, \lambda_s)\begin{pmatrix} e_s \\ n_s \\ u_s \end{pmatrix} \tag{17}$$

$$\begin{pmatrix} X_{t'} \\ Y_{t'} \\ Z_{t'} \end{pmatrix} = \begin{pmatrix} X_t \\ Y_t \\ Z_t \end{pmatrix} + R(\varphi_t, \lambda_t)\begin{pmatrix} e_t \\ n_t \\ u_t \end{pmatrix} \tag{18}$$

where $(e_s, n_s, u_s)^T$ and $(e_t, n_t, u_t)^T$ are the vectors describing the displacement of the instrument centers from the geodetic marks in their respective local systems; and $R(\varphi, \lambda)$ is the rotation matrix that converts the vector of displacement into the general ECEF system

$$R(\varphi, \lambda) = \begin{pmatrix} -\sin\lambda & -\sin\varphi\cos\lambda & \cos\varphi\cos\lambda \\ \cos\lambda & -\sin\varphi\sin\lambda & \cos\varphi\sin\lambda \\ 0 & \cos\varphi & \sin\varphi \end{pmatrix} \tag{19}$$

$R(\varphi, \lambda)$ can be evaluated by using the geodetic coordinates of the respective mechanical centers with no significant loss of accuracy.

The vectors of displacement, which are usually described in terms of easting, northing, and upping local components (e, n, and u), must be accurately measured in the field to obtain a precise correction. They define the correction vectors $\vec{c_s}$ and $\vec{c_t}$ (Fig. 12)

$$\vec{c_s} = \begin{pmatrix} \Delta X_{ss'} \\ \Delta Y_{ss'} \\ \Delta Z_{ss'} \end{pmatrix} = R(\varphi_s, \lambda_s)\begin{pmatrix} e_s \\ n_s \\ u_s \end{pmatrix} \tag{20}$$

$$\vec{c_t} = \begin{pmatrix} \Delta X_{tt'} \\ \Delta Y_{tt'} \\ \Delta Z_{tt'} \end{pmatrix} = R(\varphi_t, \lambda_t)\begin{pmatrix} e_t \\ n_t \\ u_t \end{pmatrix} \tag{21}$$

that are conveniently grouped in a unique vector $\vec{c}_{\text{offset}} = \vec{c_t} - \vec{c_s}$ and subsequently used to determine the components of the vector $\overrightarrow{cd}$ connecting the instruments centers s' and t' in the ECEF system

$$\overrightarrow{cd} = \begin{pmatrix} \Delta X_{s't'} \\ \Delta Y_{s't'} \\ \Delta Z_{s't'} \end{pmatrix} = \overrightarrow{pd} + \vec{c}_{\text{offset}}$$
$$= \begin{pmatrix} \Delta X_{st} \\ \Delta Y_{st} \\ \Delta Z_{st} \end{pmatrix} + R(\varphi_t, \lambda_t)\begin{pmatrix} e_t \\ n_t \\ u_t \end{pmatrix} - R(\varphi_s, \lambda_s)\begin{pmatrix} e_s \\ n_s \\ u_s \end{pmatrix} \tag{22}$$

Now, the geometrical correction c is straightforwardly computed

$$c = \|\overrightarrow{pd}\| - \|\overrightarrow{cd}\|$$
$$= (\Delta X_{st}^2 + \Delta Y_{st}^2 + \Delta Z_{st}^2)^{\frac{1}{2}} - (\Delta X_{s't'}^2 + \Delta Y_{s't'}^2 + \Delta Z_{s't'}^2)^{\frac{1}{2}} \quad (23)$$

In addition, the uncertainty of the geometrical correction is also required. For the sake of conciseness, the processed followed is described in three steps.

First, the precision of the vector $\overrightarrow{pd}$ is estimated by propagating the errors of the approximate geodetic coordinates of the mechanical centers as follows:

$$\Sigma_{\overrightarrow{pd}} = J_{\lambda_s\varphi_s h_s}^{X_sY_sZ_s} \Sigma_{\lambda_s\varphi_s h_s} (J_{\lambda_s\varphi_s h_s}^{X_sY_sZ_s})^T + J_{\lambda_t\varphi_t h_t}^{X_tY_tZ_t} \Sigma_{\lambda_t\varphi_t h_t} (J_{\lambda_t\varphi_t h_t}^{X_tY_tZ_t})^T \quad (24)$$

where Σ_{XYZ} is the covariance matrix of the ECEF coordinates; $\Sigma_{\varphi\lambda h}$ the covariance matrix of the approximate geodetic coordinates [with assumed errors σ_λ and σ_φ (rad) and σ_h (m)], and $J_{\varphi\lambda h}^{XYZ}$, the Jacobian that relates the corresponding differentials ($d\lambda$, $d\varphi$, dh) and (dX, dY, dZ)

$$J_{\varphi\lambda h}^{XYZ} = \begin{pmatrix} -(\nu+\mathrm{h})\cos\varphi\sin\lambda & -(\rho+\mathrm{h})\sin\varphi\cos\lambda & \cos\varphi\cos\lambda \\ (\nu+\mathrm{h})\cos\varphi\cos\lambda & -(\rho+\mathrm{h})\sin\varphi\sin\lambda & \cos\varphi\sin\lambda \\ 0 & (\rho+\mathrm{h})\cos\varphi & \sin\varphi \end{pmatrix} \quad (25)$$

where $\nu = a(1-e^2\sin^2\varphi)^{-1/2}$ and $\rho = a(1-e^2)(1-e^2\sin^2\varphi)^{-3/2}$ are the Earth's prime-vertical and meridional radius of curvature, respectively.

Second, the precision of the vector $\vec{c}$ is estimated by propagating the errors of the approximate geodetic coordinates of the mechanical centers

$$\Sigma_{\vec{c}} = R(\varphi_s, \lambda_s)\Sigma_{e_sn_su_s}(R(\varphi_s, \lambda_s))^T + R(\varphi_t, \lambda_t)\Sigma_{e_tn_tu_t}(R(\varphi_t, \lambda_t))^T \quad (26)$$

where $\Sigma_{e_sn_su_s}$ and $\Sigma_{e_tn_tu_t}$ are the covariance matrices of the measured vectors of displacement measured in the field [with assumed errors σ_e, σ_n, and σ_u (m)].

Third, the errors contained in both $\Sigma_{\overrightarrow{pd}}$ and $\Sigma_{\vec{c}}$ are finally propagated by using the Jacobian matrix of Eq. (22). Taking into consideration that for distances below 10 km and correction vectors below some decimeters, $\|\overrightarrow{pd}\| \cong \|\overrightarrow{cd}\|$, the final expression can be simplified so that only the approximate coordinates of the geodetic marks are required, as follows:

$$J_{\overrightarrow{pd},\vec{c}}^{c} = \left(\frac{\Delta X_{st}}{\|\overrightarrow{pd}\|} \quad \frac{\Delta Y_{st}}{\|\overrightarrow{pd}\|} \quad \frac{\Delta Z_{st}}{\|\overrightarrow{pd}\|} - \frac{\Delta X_{st}}{\|\overrightarrow{pd}\|} \quad -\frac{\Delta Y_{st}}{\|\overrightarrow{pd}\|} \quad -\frac{\Delta Z_{st}}{\|\overrightarrow{pd}\|} \right) \quad (27)$$

Finally, the variance of correction c is obtained as follows:

$$s_c^2 = J_{\overrightarrow{pd},\vec{c}}^{c} \begin{pmatrix} \Sigma_{\overrightarrow{pd}} & 0 \\ 0 & \Sigma_{\vec{c}} \end{pmatrix} (J_{\overrightarrow{pd},\vec{c}}^{c})^T \quad (28)$$

Appendix II. CERN Socket

The CERN sockets are the interfaces used on each pillar to receive an instrument, a target, or a GNSS antenna. This consists of a bore with a diameter of 30 mm sealed into a pillar. The upper part is designed to hold a 88.9 mm (3.5-in.) sphere or a forced-centering mount, and therefore has a conical surface (surface of the forced-centering mount is spherical so that the contact between the two is a circle). Fig. 13 shows the combination of adapters used and the location of the reference point for each pillar.

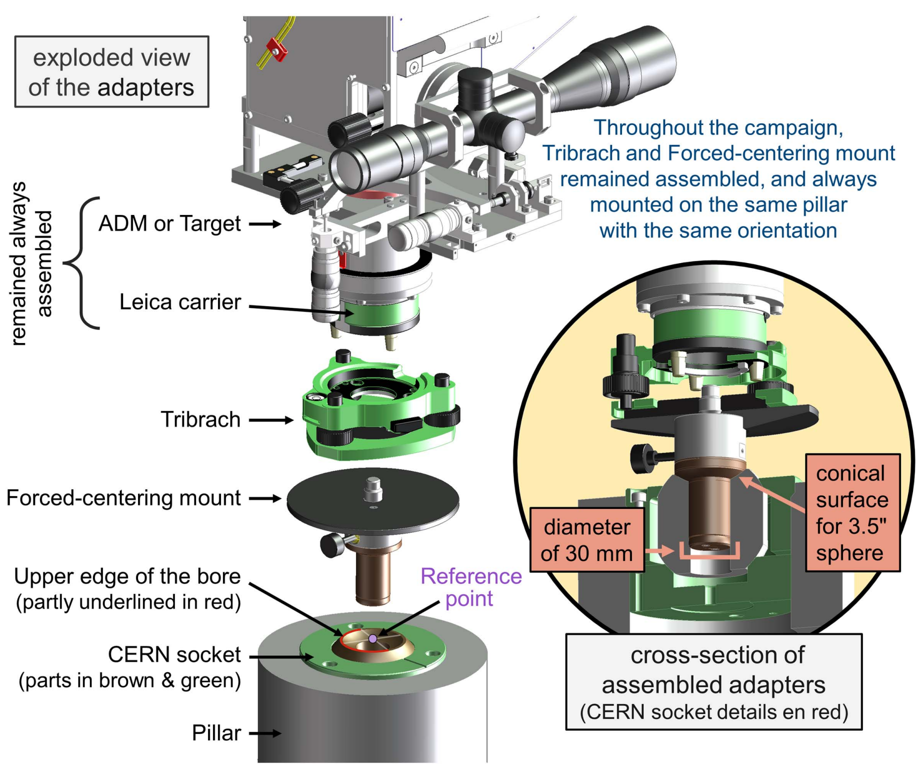

Fig. 13. Detailed views of the combination of adapters used on each pillar.

Data Availability Statement

Some data, models, or code generated or used during the study are available from the corresponding author by reasonable request. This includes the station observation data, which can be made available upon reasonable request.

Acknowledgments

This work was partially funded by the Joint Research Project (JRP) 18SIB01 GeoMetre. This project has received funding from the European Metrology Programme for Innovation and Research (EMPIR, funder ID 10.13039/100014132), cofinanced by the participating states and from the European Union's Horizon 2020 research and innovation program. This work was partially funded by the project Development of High-Precision GNSS Techniques for Dimensional Metrology, Deformation Monitoring, and Geodetic Networks for Civil Engineering Projects (GNSS-Metrology), ref. PID2022-142363NB-I00, *Plan Estatal de Investigación Científica y Técnica y de Innovación 2021-2023*, MCIN/AEI/10.13039/501100011033/FEDER, UE.

References

Banville, S., E. Hassen, P. Lamothe, J. Farinaccio, B. Donahue, Y. Mireault, M. A. Goudarzi, P. Collins, R. Ghoddousi-Fard, and O. Kamali. 2021. "Enabling ambiguity resolution in CSRS-PPP." *Navigation* 68 (2): 433–451. https://doi.org/10.1002/navi.423.

Baselga, S., L. García-Asenjo, P. Garrigues, and R. Luján. 2022. "GBDM+: An improved methodology for a GNSS-based distance meter." *Meas. Sci. Technol.* 33 (8): 085020. https://doi.org/10.1088/1361-6501/ac6f45.

Beissner, K. 2002. "On a measure of consistency in comparison measurements." *Metrologia* 39 (1): 59–63. https://doi.org/10.1088/0026-1394/39/1/8.

Bönsch, G., and E. Potulski. 1998. "Measurement of the refractive index of air and comparison with modified Edlén's formulae." *Metrologia* 35 (2): 133–139. https://doi.org/10.1088/0026-1394/35/2/8.

Ciddor, P. E., and R. J. Hill. 1999. "Refractive index of air. 2. Group index." *Appl. Opt.* 38 (9): 1663–1667. https://doi.org/10.1364/AO.38.001663.

Edlén, B. 1966. "The refractive index of air." *Metrologia* 2 (2): 71–80. https://doi.org/10.1088/0026-1394/2/2/002.

García-Asenjo, L., S. Baselga, C. Atkins, and P. Garrigues. 2021. "Development of a submillimetric GNSS-based distance meter for length metrology." *Sensors* 21 (4): 1145. https://doi.org/10.3390/s21041145.

García-Asenjo, L., S. Baselga, P. Garrigues, R. Luján, D. Pesce, B. Weyer, J. F. Fuchs, and D. Missiaen. 2022. "Application of GNSS length metrology to CERN geodetic network." Accessed January 25, 2024. https://indico.cern.ch/event/1136611/contributions/5020510.

Gervaise, J. 1983. "First results of the geodetic measurements carried out with the Terrameter, two wavelength electronic distance measurement instrument." Accessed January 25, 2024. https://doczz.com.br/doc/1162343/schriftenreihe.

Guillory, J., D. Truong, J.-P. Wallerand, and C. Alexandre. 2024. "A submillimetre two-wavelength EDM that compensates the air refractive index: Uncertainty and measurements up to 5 km." *Meas. Sci. Technol.* 35 (2): 025024. https://doi.org/10.1088/1361-6501/ad0a22.

Huggett, G. R. 1981. "Two-color terrameter." *Tectonophysics* 71 (1–4): 29–39. https://doi.org/10.1016/0040-1951(81)90044-5.

IAG (International Association of Geodesy). 1999. "Resolutions adopted at the XXIIth general assembly in Birmingham." Accessed January 25, 2024. https://office.iag-aig.org/doc/5d7b8fda0c032.pdf.

Johnston, G., A. Riddell, and G. Hausler. 2017. "The international GNSS service." In *Springer handbook of global navigation satellite systems*, edited by P. J. G. Teunissen and O. Montenbruck, 967–982. Cham, Switzerland: Springer. https://doi.org/10.1007/978-3-319-42928-1.

Jones, M., and D. Missiaen. 2018. "Geodetic activities at CERN for current and future projects." Accessed January 25, 2024. https://indico.fnal.gov/event/16262/contributions/36411/.

Meiners-Hagen, K., and A. Abou-Zeid. 2008. "Refractive index determination in length measurement by two-colour interferometry." *Meas. Sci. Technol.* 19 (8): 084004. https://doi.org/10.1088/0957-0233/19/8/084004.

Minoshima, K., K. Arai, and H. Inaba. 2011. "High-accuracy self-correction of refractive index of air using two-color interferometry of optical frequency combs." *Opt. Express* 19 (27): 26095–26105. https://doi.org/10.1364/OE.19.026095.

Pollinger, F., et al. 2023. "The European GeoMetre project: Developing enhanced large-scale dimensional metrology for geodesy." *Appl. Geomat.* 15 (2): 371–381. https://doi.org/10.1007/s12518-022-00487-3.

Ray, P., D. Salido-Monzú, and A. Wieser. 2023. "High-precision intermode beating electro-optic distance measurement for mitigation of atmospheric delays." *J. Appl. Geod.* 17 (2): 93–101. https://doi.org/10.1515/jag-2022-0039.

Röse, A., et al. 2022. "Two multi-wavelength interferometers for large-scale surveying." In *Proc., 5th Joint Int. Symp. on Deformation Monitoring (JISDM)*. Valencia, Spain: Editorial Universitat Politècnica de València.

Voronin, A. A., and A. M. Zheltikov. 2017. "The generalized Sellmeier equation for air." *Sci. Rep.* 7 (1): 46111. https://doi.org/10.1038/srep46111.